



## Novel alpha-7-oxy-4-(4-methoxyphenyl)-8-methylcoumarin substituted metal-free, Co(II) and Zn(II) phthalocyanines: Photochemistry, photophysics, conductance and electrochemistry

Zafer Odabaş<sup>a</sup>, Efe Baturhan Orman<sup>a</sup>, Mahmut Durmuş<sup>b</sup>, Fatih Dumludag<sup>c</sup>, Ali Rıza Özkaya<sup>a,\*</sup>, Mustafa Bulut<sup>a,\*</sup>

<sup>a</sup>Department of Chemistry, Marmara University, Kadıköy, 34722 Göztepe-Istanbul, Turkey

<sup>b</sup>Department of Chemistry, Gebze Institute of Technology, P.O. Box 141, Gebze 41400, Kocaeli, Turkey

<sup>c</sup>Department of Physics, Marmara University, Kadıköy 34722, Göztepe-Istanbul, Turkey

### ARTICLE INFO

#### Article history:

Received 2 April 2012

Received in revised form

21 May 2012

Accepted 22 May 2012

Available online 7 June 2012

#### Keywords:

Phthalocyanine  
Electrochemistry  
J-aggregation  
Photophysics  
Semiconductor  
Photochemistry

### ABSTRACT

Novel alpha-substituted metal-free, Co(II) and Zn(II) phthalocyanines, bearing four 7-oxy-4-(4-methoxyphenyl)-8-methylcoumarin moieties were synthesized. The compounds were characterized by elemental analysis, IR, UV–vis, <sup>1</sup>H NMR, <sup>13</sup>C NMR and MALDI-TOF mass spectroscopies. The Zn(II) phthalocyanine compound showed J-type aggregation in non-coordinating solvents. The photophysical and photochemical properties of these compounds were described in different solvents. Direct current conductivity measurements of the films of Co(II) and Zn(II) phthalocyanines as a function of temperature showed that these compounds are semiconductors with the activation energies within the range of 0.40–0.84 eV. The variation of alternating current conductivity of the films with frequency was found to be represented by the function  $\sigma_{AC} = A\omega^S$ . The results indicated that charge transport mechanism of the films can be explained by hopping. The redox properties of the compounds were also examined in dimethylsulfoxide and dichloromethane by voltammetry and *in situ* spectroelectrochemistry. The compounds displayed metal and/or phthalocyanine ring-based reduction and oxidation processes. The electrochemistry of a phthalocyanine compound forming a J-aggregated species has been investigated. It was found that some redox couples of the Zn(II) compound in dichloromethane is split due to the equilibrium between its aggregated and non-aggregated species.

© 2012 Elsevier Ltd. All rights reserved.

### 1. Introduction

Phthalocyanines (Pcs) are composed of four iminoisindoline units where the pyrrole groups are conjugated to benzene rings and bridged by azanitrogens. Pcs have highly coloured, planar and 18 $\pi$ -electron heterocyclic aromatic systems [1]. A great number of unique properties arise from this electronic delocalization that makes these compounds valuable in different fields of technology as pigments, dyes, sensors, photodynamic therapy of cancer, optical recording and non-linear optical materials, electronic device components photovoltaics, catalysts and electrochromism [1–4]. It is well known that nearly all technologically important properties of Pc derivatives can be tuned by varying the central metal atom, changing the size of the  $\pi$ -conjugated system, or alternating

the type, number, and positions of the substituents on the macrocycle.

Supramolecular self-assembly is a very useful technique to fabricate molecular materials and molecular machines to perform specific functions such as chemical sensing, electrical conductivity, and mechanical movements. In the case of Pcs, self-aggregation that forms dimers and high order aggregates has been extensively investigated. The driving force for such aggregation involves ligand-metal coordination,  $\pi$ -stacking, hydrogen bonding and donor–acceptor interactions. It has been established that Pcs can form H- and J-aggregates depending on the orientation of the induced transition dipoles of their constituent monomers. In H-aggregates, the component monomers are arranged into a face-to-face conformation, and transition dipoles are perpendicular to the line connecting their centers. In contrast, in J-aggregates, the component monomers adopt a side-by-side conformation, and their transition dipoles are parallel to the line connecting their centers. Except for a few examples, usually, H-aggregates of Pcs have been observed [5]. The high H-aggregation tendency of Pc

\* Corresponding authors. Tel.: +90 216 347 96 41; fax: +90 216 347 87 83.

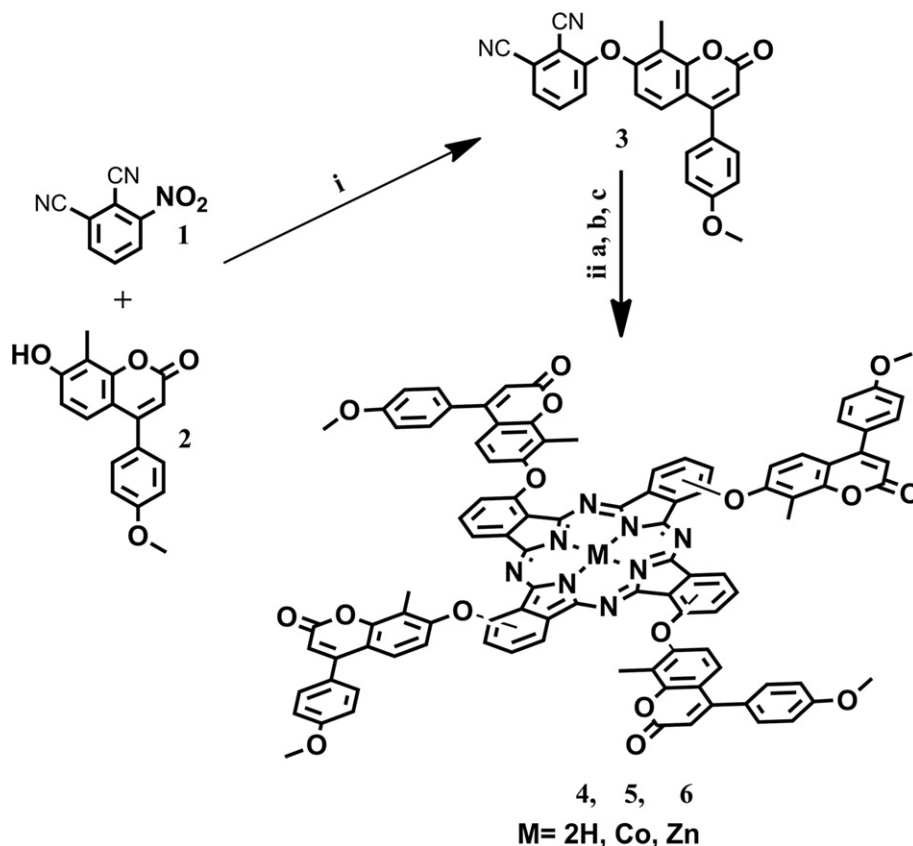
E-mail addresses: [aliozkaya@marmara.edu.tr](mailto:aliozkaya@marmara.edu.tr) (A.R. Özkaya), [mbulut@marmara.edu.tr](mailto:mbulut@marmara.edu.tr) (M. Bulut).

compounds, especially  $\beta$ -substituted ones, through the intermolecular interactions between their rings usually causes these compounds to be insoluble or have limited solubility in many solvents [6] and thus, complicate the detection of their physicochemical properties [7]. Furthermore, the intermolecular interactions resulting from this phenomenon can dramatically affect their photophysical [8], photochemical [9], electrical [10] and electrochemical [11] properties. For instance, H-aggregation has been found to cause decrease in their light absorption and induce a large reduction in their fluorescence quantum yield [8]. On the other hand,  $\alpha$ -substituted Pcs differ significantly in their solubility, aggregation and thus various physicochemical properties, in comparison with corresponding  $\beta$ -substituted ones [12]. These compounds do not form H-aggregated species, due to their conformation deviating from planarity, and thus fluoresce. However,  $\alpha$ -substituted Pcs can form J-type aggregates in non-coordinating solvents such as chloroform, dichloromethane (DCM) or toluene. J-aggregates are highly desirable to maximize the optical properties of the organic dyes [13].

Coumarin (2H-1-benzopyran-2-one, 2H-chromen-2-one) derivatives are biologically active compounds with numerous metabolites and widespread in nature [14]. These compounds possess a significant organic fluorophore and are widely used in some applications such as synthesizing laser dyes, chemosensors for metal detections, pH sensors, liquid crystals and organic non-linear optical materials, due to their characteristics of high emission yield, excellent photostability and extended spectral range [15]. In view of the versatile importance of both coumarins and  $\alpha$ -substituted Pcs it is worthwhile to combine these two

functional groups into a single hybrid compound via synthetic methodology and characterize its metal-free and metallo derivatives, which may also exhibit high solubility in various solvents and intriguing physicochemical properties.

The synthesis and characterization of Pc compounds including different oxy-coumarin substituents have been studied previously [16–18]. Contrary to the previously reported studies, in the present work, the designed compounds formed J-aggregates and their electrochemical properties in different solvents has been discussed. Although there have been many reports on the electrochemical properties of various H-aggregated metallo Pcs [19–21], to the best of our knowledge, this is the first report investigating the redox and *in situ* spectroelectrochemical behavior of a J-aggregated metallo Pc. Novel  $\alpha$ -tetra substituted metal free, cobalt and zinc Pcs have been prepared from 3-[4-(4-methoxyphenyl)-8-methylcoumarin-7-oxy]phthalonitrile (Scheme 1) and characterized by elemental analyses, UV–vis, IR,  $^1\text{H}$  NMR,  $^{13}\text{C}$  NMR and matrix assisted laser desorption/ionization–time of flight (MALDI-TOF) mass spectroscopies. The aggregation behavior of newly synthesized compounds was investigated by UV–vis spectroscopy in different solvents such as toluene, chloroform, DCM and dimethylsulfoxide (DMSO). Photophysical (fluorescence lifetime and quantum yields) and photochemical (singlet oxygen and photodegradation quantum yields) properties were investigated in different solvents. Direct current (DC) and alternating current (AC) conductivity and impedance spectroscopy measurements of their thin films were also performed as functions of temperature and frequency under vacuum ( $\sim 2 \times 10^{-3}$  mbar) in dark with the aim of identifying the charge transport mechanism.



**Scheme 1.** Synthesis of **3**, **4**, **5** and **6**. Reagents and conditions: i.  $\text{K}_2\text{CO}_3$ ,  $\text{N}_2$ , dimethylsulfoxide,  $50^\circ\text{C}$ , 24 h; ii a) 2-N,N-dimethylaminoethanol,  $\text{N}_2$   $160^\circ\text{C}$ , 48 h, b)  $\text{Co}(\text{OAc})_2 \cdot 4\text{H}_2\text{O}$  or c)  $\text{Zn}(\text{OAc})_2 \cdot 2\text{H}_2\text{O}$ ,  $\text{N}_2$ ,  $320^\circ\text{C}$ , 20 min, respectively.

## 2. Experimental section

### 2.1. Synthesis of 3-[4-(4-methoxyphenyl)-8-methylcoumarin-7-oxy]phthalonitrile (**3**)

3-Nitrophthalonitrile (**1**) (0.86 g, 5 mmol) and 7-hydroxy-4-(4-methoxyphenyl)-8-methylcoumarin (**2**) (1.41 g, 5 mmol) were dissolved in anhydrous DMSO (20 mL). After stirring for 10 min; finely ground anhydrous  $K_2CO_3$  (2.07 g, 15 mmol) was added by stirring. The reaction mixture was stirred at 50 °C for 24 h under  $N_2$  atmosphere. The mixture was poured into ice water and the obtained precipitate was filtered off, washed by using water and dried in vacuum at 50 °C. Then it was also purified by column chromatography with silica gel eluting with  $CHCl_3$  a gradient of  $CHCl_3$ -tetrahydrofuran (THF) up to 5% THF.

Compound **3** is soluble in DCM,  $CHCl_3$ , THF, dimethylformamide (DMF), DMSO and acetic acid. Mp: 214–215 °C Yield: 1.86 g (91.18%). Anal calculated for  $C_{25}H_{16}N_2O_4$  C, 73.52%; H, 3.95%; N, 6.86%; found C, 73.41%; H, 4.08%; N, 6.72%. IR (KBr pellet)  $\nu_{max}/cm^{-1}$ : 597, 798, 895, 950, 1027, 1087, 1174, 1249, 1283, 1366, 1422, 1461, 1487, 1512, 1572, 1603, 1732, 2228, 2854, 2922, 3066.  $^1H$  NMR (500 MHz,  $CDCl_3$ ):  $\delta$ , ppm 2.42 (s, 3H), 3.87 (s, 3H), 6.38 (s, 1H), 6.89 (d,  $J = 8.98$  Hz, 1H), 7.02 (dd,  $J = 8.99$  Hz,  $J = 1.95$  Hz, 1H), 7.06 (dd,  $J = 8.59$  Hz,  $J = 1.95$  Hz, 2H), 7.41 (dd,  $J = 8.98$  Hz,  $J = 1.95$  Hz, 2H), 7.49 (d,  $J = 8.98$  Hz, 1H), 7.54 (dd,  $J = 8.59$  Hz,  $J = 1.95$  Hz, 1H), 9.76 (t, 1H).

### 2.2. Synthesis of 1(4),8(11),15(18),22(25)-tetra[4-(4-methoxyphenyl)-8-methylcoumarin-7-oxy]phthalocyanine (**4**)

Compound **3** (0.10 g, 0.25 mmol) was heated in dry 2-N,N-dimethylaminoethanol (2 mL) in a sealed tube. The mixture was held at 160 °C for 48 h under  $N_2$  atmosphere. After cooling to room temperature, the reaction mixture was treated with dilute HCl and the mixture was filtered and washed with water until the filtrate became neutral. The raw green product was taken in the soxhlet apparatus then purified by washing with hot water, acetic acid, ethanol and acetonitrile for 12 h, respectively. The product was further purified by column chromatography with silica gel eluting with  $CHCl_3$  a gradient of  $CHCl_3$ -THF up to 5% THF.

The metal free Pc **4** is soluble in  $CHCl_3$ , DCM, toluene, THF, DMF and DMSO. Mp > 300 °C. Yield: 38.0 mg (38.0%). Anal calculated for  $C_{100}H_{66}N_8O_{16}$ : C, 73.43%; H, 4.07%; N, 6.85%; found C, 73.26%; H, 3.96%; N, 7.03%. IR (KBr pellet)  $\nu_{max}/cm^{-1}$ : 529, 748, 831, 937, 1021, 1083, 1175, 1243, 1332, 1366, 1478, 1511, 1581, 1603, 1722, 2837, 2924, 3066, 3283.  $^1H$  NMR (500 MHz,  $CDCl_3$ ):  $\delta$  ppm 8.08–6.75 (m, 40H), 3.70 (s, 12H), 2.09 (s, 12H), –1.58 (s, 2H).  $^{13}C$  NMR (125 MHz,  $CDCl_3$ ):  $\delta$  ppm 161.92–110.84 (92C), 55.28 (4C), 9.69 (4C). MALDI-TOF-MS:  $m/z$  1634.67 ( $M$ )<sup>+</sup> and 1657.65 ( $M + Na$ )<sup>+</sup>, 1673.63 ( $M + K$ )<sup>+</sup>. UV–vis (DCM):  $\lambda_{max}$ (nm), (log  $\epsilon$ ): 319 (5.800), 621 (5.290), 653 (5.417), 684 (5.860), 715 (5.922).

### 2.3. Synthesis of 1(4),8(11),15(18),22(25)-tetra[4-(4-methoxyphenyl)-8-methylcoumarin-7-oxy]phthalocyaninatocobalt(II) and zinc(II) (**5** and **6**)

A mixture of compound **3** (0.10 g, 0.25 mmol) and metal salt (either 0.063 g, 0.25 mmol  $Co(OAc)_2 \cdot 4H_2O$  or 0.064 g, 0.25 mmol  $Zn(OAc)_2 \cdot 2H_2O$ ) was powdered in a quartz crucible and transferred in a reaction tube. 0.30 mL of DMF was added to this reaction mixture and the mixture was heated in a sealed glass tube for 20 min under dry  $N_2$  atmosphere at 320 °C. After cooling to room temperature, DMF (3 mL) was also added to the residue to solve the product. The reaction mixture was precipitated by adding acetic acid. The precipitate was filtered and washed with hot water, acetic

acid, ethanol and acetonitrile for 12 h respectively in the soxhlet apparatus. The product was further purified by column chromatography with silica-gel eluting with  $CHCl_3$  a gradient of  $CHCl_3$ -THF up to 5% THF.

**5**: Mp > 300 °C. Yield: 80.00 mg (77.20%). Anal calculated for  $C_{100}H_{64}CoN_8O_{16}$ : C, 70.96%; H, 3.81%; N, 6.62%; found C, 70.85%; H, 3.94%; N, 6.71%. IR (KBr pellet)  $\nu_{max}/cm^{-1}$ : 528, 566, 601, 747, 832, 957, 979, 1084, 1175, 1243, 1330, 1366, 1421, 1483, 1511, 1584, 1604, 1724, 2837, 2933, 3066. MALDI-TOF-MS:  $m/z$  1677.57 ( $M - CH_3$ )<sup>+</sup>, 1691.59 ( $M$ )<sup>+</sup> and 1714.56 ( $M + Na$ )<sup>+</sup>. UV–vis (DCM):  $\lambda_{max}$ (nm), (log  $\epsilon$ ): 317 (5.759), 618 (5.210), 685 (5.838).

**6**: Mp > 300 °C. Yield: 75.00 mg (72.20%). Anal calculated for  $C_{100}H_{64}ZnN_8O_{16}$ : C, 70.69%; H, 3.80%; N, 6.60%; found C, 70.82%; H, 3.65%; N, 6.46%. IR (KBr pellet)  $\nu_{max}/cm^{-1}$ : 529, 558, 602, 741, 831, 866, 955, 1045, 1083, 1175, 1244, 1332, 1366, 1422, 1478, 1511, 1579, 1602, 1722, 2827, 2929, 3066.  $^1H$  NMR (500 MHz,  $CDCl_3$ ):  $\delta$  ppm 8.06–6.72 (m, 40H), 3.90 (s, 12H), 2.12 (s, 12H).  $^{13}C$  NMR (125 MHz,  $CDCl_3$ ):  $\delta$  ppm 163.88–109.97 (92C), 55.32 (4C), 9.07 (4C). MALDI-TOF-MS:  $m/z$  1696.61 ( $M$ )<sup>+</sup>, 1803.44 ( $M + 2Na + CH_3COOH$ )<sup>+</sup> and 3393.19 ( $M_2$ )<sup>+</sup>. UV–vis (DCM):  $\lambda_{max}$ (nm), (log  $\epsilon$ ): 317 (5.537), 624 (4.984), 665 (4.988), 693 (5.739), 741 (4.788).

## 3. Results and discussion

### 3.1. Syntheses and characterization

The starting material, 3-[4-(4-methoxyphenyl)-8-methylcoumarin-7-oxy]phthalonitrile (**3**), was synthesized by  $K_2CO_3$  base catalyzed nucleophilic aromatic nitro displacement of 3-nitrophthalonitrile (**1**) with 7-hydroxy-4-(4-methoxyphenyl)-8-methylcoumarin (**2**) in DMSO. The novel CoPc (**5**) and ZnPc (**6**) were prepared by the templated cyclo-tetramerization reaction from compound **3** and metal salts [ $Co(OAc)_2 \cdot 4H_2O$  and  $Zn(OAc)_2 \cdot 2H_2O$ ] in DMF (0.3 mL) at 320 °C. Metal-free Pc (**4**) was also synthesized by heating compound **3** in 2-N,N-dimethylaminoethanol at 160 °C under  $N_2$  atmosphere (Scheme 1). Compounds **4–6** were purified by washing with acetic acid, hot water, ethanol and acetonitrile, respectively in the soxhlet apparatus and by column chromatography. The yields were considerably high (approximately 38% for **4**, 77% for **5** and 72% for **6**). These novel Pcs are soluble in common solvents such as toluene, chloroform, DCM, THF, DMSO and DMF.

The characterization of the new products involved a combination of methods including elemental analyses, IR, UV–vis,  $^1H$  NMR,  $^{13}C$  NMR and MALDI-TOF mass spectroscopies. Elemental analysis results and the spectral data of the newly synthesized compounds **3–6** are consistent with the proposed structures.

The FT-IR absorption spectrum of **3** exhibited two strong bands at 1732 and 1603  $cm^{-1}$ , which may be assigned to coumarin carbonyl (lactone,  $-C=O$ ) and  $\alpha,\beta$ -unsaturated  $-C=C-$  double bond (or aromatic rings  $-C=C-$ ), respectively. The bands at 3066  $cm^{-1}$  indicated Ar-H stretching frequencies. The formation of **3** was confirmed by the appearance of a new absorption band at 2228  $cm^{-1}$  ( $-C\equiv N$ ) and additional bands at 1249  $cm^{-1}$  (Ar–O–Ar) in the FT-IR spectrum. The IR spectra of **4**, **5** and **6** were very similar, but compound **4** showed an extra weak N–H stretching band at 3283  $cm^{-1}$  due to the inner core.

The molecular ion peaks [ $M$ ]<sup>+</sup> of the Pc compounds **4**, **5** and **6** were identified easily with  $\alpha$ -cyano-4-hydroxycinnamic acid (ACCA) MALDI matrix in the reflectron mode by using MALDI-TOF mass spectrometry. The molecular ion peak of **4** was observed at 1634.67 [ $M$ ]<sup>+</sup>. Beside the molecular ion peak of the complexes, sodium and potassium adducts were observed at 1657.85 and 1673.63 respectively (Supplementary material, Fig. S1). The molecular ion peak of **5** was observed at 1691.59 Da. Two intense

peaks were also observed at 1677.57  $[M - CH_3]^+$  and 1714.56 Da  $[M + Na]^+$  (Supplementary material, Fig. S2). The molecular ion peak of **6** was observed at 1696.61 Da. The extra aggregate dimer peak was also observed at 3393.19  $[M_2]^+$  (Fig. 1). The molecular ion peaks of the complexes overlapped with the theoretical calculated mass values of the complexes.

The  $^1H$  NMR spectrum of **3** exhibited characteristic signals for methyl ( $-CH_3$ ) and  $-OCH_3$  protons at  $\delta$  2.42 and  $\delta$  3.87 ppm, respectively, each as a singlet. The peaks at  $\delta$  6.38 and between  $\delta$  6.89–9.76 ppm indicated the presence of protons at lactone ring and the aromatic protons, respectively (Supplementary material, Fig. S3). In the  $^1H$  NMR spectra of **4** and **6**, the aromatic,  $-OCH_3$ ,  $-CH_3$  and  $-NH$  protons of **4** appeared between 8.08 and 6.75 ppm (m), and at 3.70 ppm (s), 2.09 ppm (s) and  $-1.58$  ppm (bs), respectively and the aromatic,  $-OCH_3$  and  $-CH_3$  protons of the compound **6** were observed between 8.06 and 6.72 ppm (m), at 3.90 ppm (s) and at 2.12 ppm (s), respectively (Supplementary material, Figs. S4 and S5).

In the  $^{13}C$  NMR spectra of **4** and **6**, the aromatic,  $-OCH_3$ , and  $-CH_3$  carbon atoms of **4** appeared at 161.92–110.84 ppm, 55.28 ppm, and 9.69 ppm, respectively, whereas the aromatic,  $-OCH_3$  and  $-CH_3$  carbon atoms of **6** were observed at 163.88–109.97 ppm, 55.32 ppm and 9.07 ppm, respectively (Supplementary material, Figs. S6 and S7).

Electronic absorption behavior of **4–6** has been examined by UV–vis spectroscopy in different solvents. The split Q band of **4** in toluene, DCM and chloroform is characteristic for the  $D_{2h}$  symmetry of monomeric metal-free Pcs (Supplementary material, Fig. S8). There is also a set of weaker vibronic satellite bands at shorter wavelengths. The split Q band converted to single band in DMF and DMSO, suggesting that deprotonation of the inner pyrrolic H atoms in the Pc core and thus, symmetry change from  $D_{2h}$  to  $D_{4h}$  occurs due to basicity of these solvents [22–24]. Compound **5** gave electronic spectra involving a single narrow and non-split Q band, typical of metal Pc complexes (Supplementary material, Fig. S9) in DMSO, DMF, toluene, DCM and chloroform. The presence of Pc aggregates can be observed in the Q-band region of the electronic absorption spectrum since upon formation of higher order complexes, the coupling between the electronic states of individual monomeric Pc units causes significant spectral perturbations. It has been established that Pcs usually form H-aggregates with the arrangement of the component monomers into a face-to-face conformation [5,25]. This results in a decrease in intensity of

strong Q band absorption corresponding to the monomeric species, meanwhile a new, broader and blue-shifted band is seen to increase in intensity. Therefore, the narrow and sharp Q-bands in the electronic spectra of **4** and **5** in toluene, DCM and chloroform are typical of non-aggregated species. The electronic spectra of **6** in DMSO and DMF also display monomeric behavior (Fig. 2). However, in addition to the normal Q band, an unusual red-shifted sharp band at 740 nm is observed in DCM, chloroform and toluene.

This band should be due to the presence of J-aggregated species since it is well known from literature that zinc Pc complexes involving ether oxygen atoms usually display J-aggregation behavior [5,8,24]. Complementary coordination of the linking oxygen atoms in one molecule of **6** (etheric oxygens and/or lactone oxygens) with the core Zn(II) ion of its another molecule should be responsible for the formation of J-aggregates [5]. The J-aggregation behavior of **6** was also supported by the appearance of a peak at 3393.19 Da in its MALDI-TOF mass spectrum (Fig. 1). The reason for the formation of J-aggregates of only **6** may be stronger coordinating ability of zinc atom than hydrogen and cobalt atoms. The gradual addition of DMSO to the solution of **6** in chloroform caused an increase in the absorption of the monomer band at 693 nm and a decrease in that of the J-band at 740 nm followed by its disappearance (Supplementary material, Fig. S10). These spectral changes suggested clearly that the addition of a coordinating solvent caused disaggregation of the J-aggregated species as a result of the competitive coordination of the solvent molecules to central zinc atoms. Monomer and J-aggregated dimer films of **6** were also obtained by spraying their solutions on glass. The evidence for the formation of J-type network structures of **6** in non-coordinating solvents based on electronic absorption spectroscopy as well as MALDI-TOF mass spectroscopy were further strengthened by a scanning electron microscopy (SEM) study. Fig. 3 shows the SEM images of the sprayed film prepared from aggregated solution of **6** with a stick-like morphology with long and thin fibrils (around 80 nm thick) forming one dimensional bundle. This morphology was not observed with the film of **6**, prepared from its solution involving monomer species.

### 3.2. Photophysical and photochemical properties

The fluorescence behavior of **4** and **6** was studied in different solvents (toluene, chloroform, DCM and DMSO). Complex **5** is not fluorescence due to paramagnetic properties of central cobalt atom. Fig. 4 shows the absorption, fluorescence emission and excitation

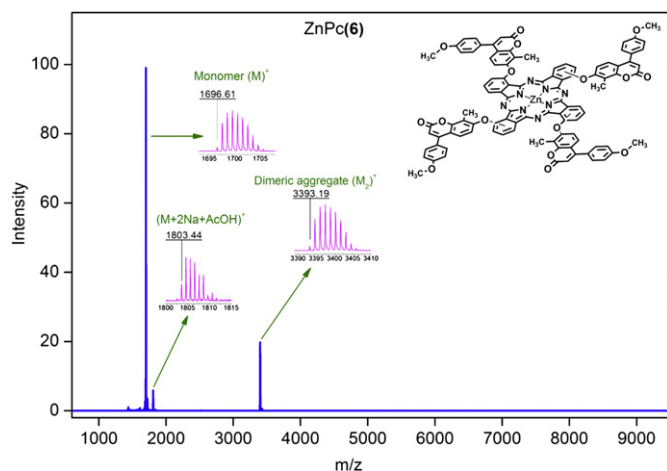


Fig. 1. Positive ion and reflectron mode MALDI-TOF-MS spectrum of **6** in  $\alpha$ -cyano-4-hydroxycinnamic acid MALDI matrix using nitrogen laser (at 337 nm wavelength) accumulating 50 laser shots.

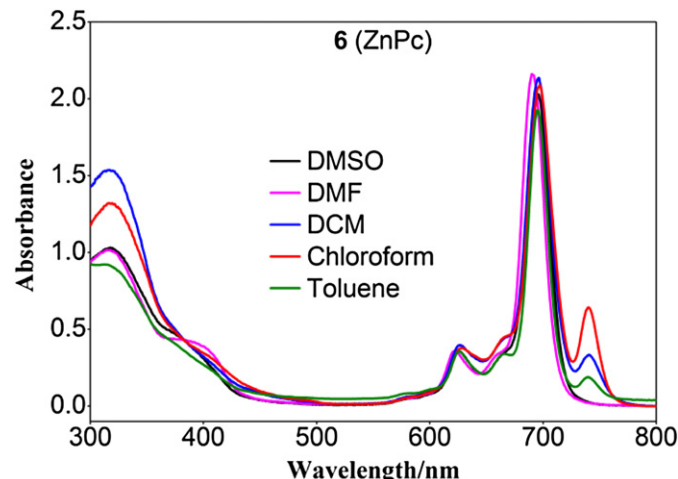


Fig. 2. Absorption spectra of  $8.0 \times 10^{-6}$  M **6** in different solvents.

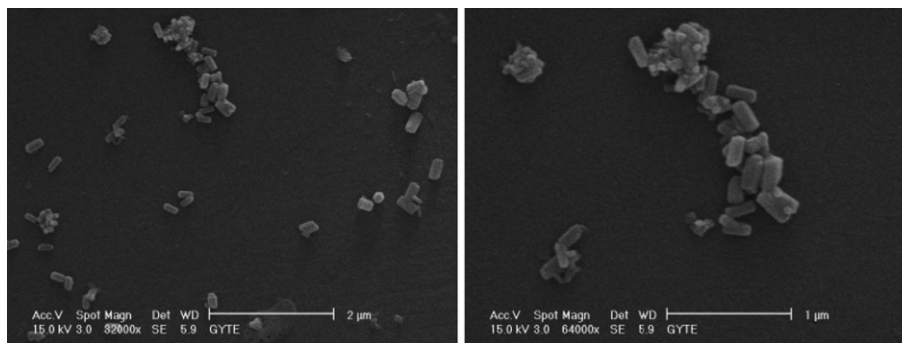


Fig. 3. SEM images of the sprayed film (gold-stained) of **6** on glass.

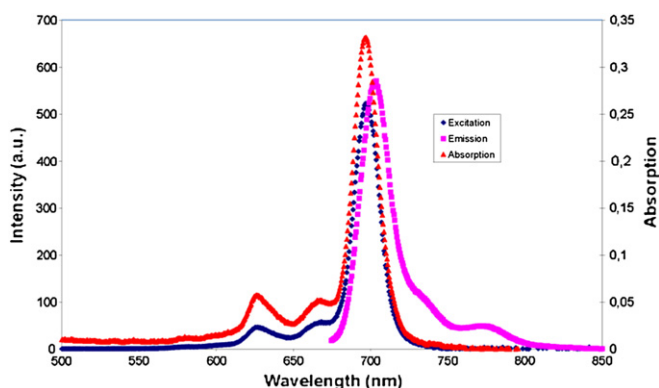


Fig. 4. Absorption, fluorescence emission and excitation spectra of **6** in toluene.

spectra of **6** in toluene, as an example. The shapes of the excitation spectra were similar to absorption spectra for **4** (Supplementary material, Fig. S11) and **6** (Fig. 4) in all studied solvents suggesting that the molecules did not show any degradation during excitation. Fluorescence emission and excitation peaks in different solvents are listed in Table 1. While the observed Stokes shifts of **6** are similar, Stokes shifts of **4** are lower than Pc derivatives having different substituents on the Pc ring in the literature [26]. The Stokes shifts of the substituted **6** are higher than those of **4** in all studied solvents (Table 1).

The fluorescence quantum yields ( $\Phi_F$ ) of **4** and **6** are typical of Pc complexes in all studied solvents. Compound **4** shows larger  $\Phi_F$  values than **6** in all studies solvents (Table 2). Lifetimes of fluorescence ( $\tau_F$ , Table 2) were calculated using the natural radiative

lifetime ( $\tau_0$ ) by the Strickler-Berg equation (Supplementary material, Eq.(2)). A good correlation was found between experimentally and the theoretically determined lifetimes for the Pc molecules, as reported in a literature example [27]. Generally, the  $\tau_F$  values are within the range reported for MPc complexes [26].  $\tau_F$  values are longer for **4** when compared to **6** in all studied solvents (Table 2). The natural radiative lifetimes ( $\tau_0$ ) and the rate constants for fluorescence ( $k_F$ ) values of **4** and **6** in different solvents are also given in Table 2.  $\tau_0$  values of **4** and **6** are longest in DMSO. There was no clear trend for the natural radiative lifetimes ( $\tau_0$ ) and rate constants for fluorescence ( $k_F$ ) values of **4** and **6**.

The singlet oxygen quantum yield, ( $\Phi_\Delta$ ) values of **4**, **5** and **6** were determined in DMSO and toluene using a chemical method. These values could not be investigated in chloroform and DCM due to the lack of a standard in these solvents. There was no decrease in the Q band or formation of new bands during  $\Phi_\Delta$  determinations, as shown in Fig. 5 for **6** in toluene as an example. This indicates that the Pcs are not degraded during singlet oxygen studies. It is believed that during photosensitization, the Pc is firstly excited to the singlet state and through intersystem crossing reaches the triplet state, then it transfers energy to ground state oxygen,  $O_2(^3\Sigma_g^-)$ , and converts itself into its excited state (singlet oxygen),  $O_2(^1\Delta_g)$ . This singlet oxygen is the chief cytotoxic species, which subsequently oxidizes the surrounding substrates: this oxidation is the key of the Type II mechanism [28]. The  $\Phi_\Delta$  values of **6** are higher when compared to **4** and **5** in both toluene and DMSO. The  $\Phi_\Delta$  values of **5** are very low due to paramagnetic properties of the central cobalt atom (Table 2).

The spectral changes observed for all Pcs (**4**, **5** and **6**) during irradiation are as shown in Fig. 6 (using complex **4** in chloroform as an example). For all substituted Pcs in all studied solvents, the collapse of the absorption spectra without any distortion of the

Table 1  
Spectral data for Pcs **4–6** in various solvents at  $3.0 \times 10^{-6}$  M.

Solvent	Pcs	Q band, $\lambda_{max}/nm$	Log $\epsilon$	B-band, $\lambda_{max}/nm$	Log $\epsilon$	Excitation $\lambda_{Ex}$ (nm)	Emission $\lambda_{Em}$ (nm)	Stokes shift $\Delta_{Stokes}$ (nm)
Toluene	<b>4</b>	716, 685, 653, 621	5.970, 5.906, 5.397, 5.270	314	5.763	685, 717	722	5
CHCl <sub>3</sub>	<b>4</b>	718, 685, 653, 620	5.841, 5.764, 5.237, 5.067	322	5.637	686, 718	723	5
DCM	<b>4</b>	715, 685, 653, 621	5.922, 5.860, 5.417, 5.290	319	5.800	685, 716	721	5
DMSO	<b>4</b>	689, 658, 631	5.681, 5.354, 5.268	318	5.724	695, 722	726	4
Toluene	<b>5</b>	685, 617	5.819, 5.171	289	5.988	–	–	–
CHCl <sub>3</sub>	<b>5</b>	684, 617	5.907, 5.248	318	5.806	–	–	–
DCM	<b>5</b>	685, 618	5.838, 5.210	317	5.759	–	–	–
DMSO	<b>5</b>	676, 613	5.744, 5.208	319	5.766	–	–	–
Toluene	<b>6</b>	740, 693, 664, 624	4.727, 6.003, 5.204, 5.230	315	5.732	694	702	8
CHCl <sub>3</sub>	<b>6</b>	740, 694, 663, 626	5.408, 5.758, 5.127, 5.011	316	5.549	694	704	10
DCM	<b>6</b>	741, 693, 665, 624	4.788, 5.739, 4.988, 4.984	317	5.537	694	703	10
DMSO	<b>6</b>	695, 662, 626	5.755, 4.988, 5.006	325	5.540	697	707	10

**Table 2**  
Photophysical and photochemical data for Pcs 4–6 in various solvents.

Solvent	Pcs	$\Phi_F$	$\tau_F$ (ns)	$\tau_0$ (ns)	$^a k_F$ ( $s^{-1}$ ) ( $\times 10^8$ )	$\Phi_d$ ( $\times 10^{-5}$ )	$\Phi_\Delta$
Toluene	4	0.18	0.91	5.03	1.99	1.16	0.31
CHCl <sub>3</sub>	4	0.23	1.87	8.15	1.22	1.76	–
DCM	4	0.21	1.04	4.96	2.01	1.18	–
DMSO	4	0.19	1.72	9.06	1.10	2.75	0.21
Toluene	5	–	–	–	–	1.67	0.0064
CHCl <sub>3</sub>	5	–	–	–	–	9.29	–
DCM	5	–	–	–	–	3.12	–
DMSO	5	–	–	–	–	1.07	0.012
Toluene	6	0.16	0.84	5.27	1.89	0.97	0.57
CHCl <sub>3</sub>	6	0.16	0.73	4.57	2.18	0.020	–
DCM	6	0.15	0.73	4.85	2.06	0.015	–
DMSO	6	0.16	1.32	8.26	1.21	1.47	0.78

<sup>a</sup>  $k_F$  is the rate constant for fluorescence. The values were calculated using  $k_F = \Phi_F / \tau_F$ .

shape confirms photodegradation which is not associated with phototransformation. The photodegradation quantum yield ( $\Phi_d$ ) values of **4**, **5** and **6** in different solvents are given in Table 2. All the complexes showed about the same stability with  $\Phi_d$  of the order of  $10^{-5}$ . It was reported in literature that stable Pc molecules show  $\Phi_d$  values as low as  $10^{-6}$  and unstable ones show  $\Phi_d$  values of the order of  $10^{-3}$  [26]. The  $\Phi_d$  values, found in this study, are similar with zinc Pc derivatives having different substituents on the Pc ring in the literature [26]; except those of **6** in both chloroform and DCM suggesting that complex **6** forms J-aggregated species in these solvents.

### 3.3. Electrical properties

#### 3.3.1. DC properties

DC conductivity studies were performed on the films of **5** and **6** at different temperatures during heating from 295 K to 523 K under vacuum ( $\sim 2 \times 10^{-3}$  mbar) in the dark. Current values passing through the films were recorded versus (vs.) applied voltages. DC conductivity values were determined using the I–V curves and found to be  $1.58 \times 10^{-10}$  S/cm for the film of **5** and  $3.16 \times 10^{-10}$  S/cm for the film of **6** at 295 K, respectively. These values increased to the values of  $5.86 \times 10^{-5}$  S/cm and  $3.70 \times 10^{-5}$  S/cm at 523 K, for the films of **5** and **6**, respectively. The value for the film of **5** ( $1.58 \times 10^{-10}$  S/cm) at room temperature is greater than that ( $3.84 \times 10^{-12}$  S/cm) reported [29] for the unsubstituted cobalt Pc.

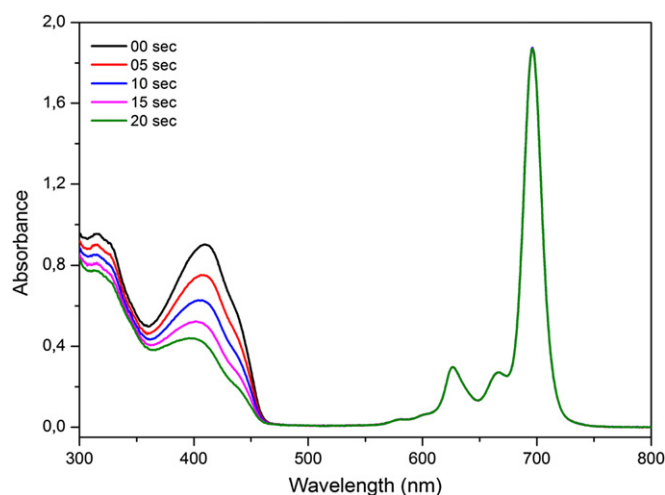


**Fig. 5.** Absorption spectral changes during the determination of singlet oxygen quantum yield of **6** in toluene at a concentration of  $1 \times 10^{-5}$  M.

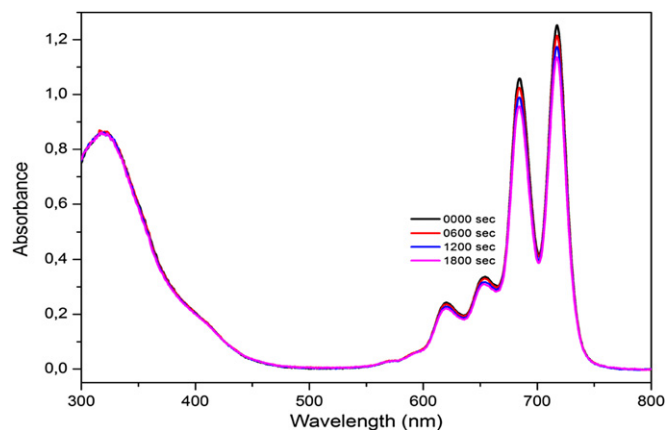


**Fig. 6.** Absorption spectral changes of Pc complex **4** in chloroform under light irradiation showing the disappearance of the Q band at 10 min intervals.

The value of  $3.16 \times 10^{-10}$  S/cm for the film of **6** at room temperature is also higher than the reported [30] value ( $2.6 \times 10^{-11}$  S/cm) for an ortho-chloranil doped non-substituted zinc Pc and nearly in equal order with that reported for non-substituted zinc Pc [31]. The higher conductivity values of **5** and **6** may arise from alpha-7-oxy-4-(4-methoxyphenyl)-8-methylcoumarin substituents in the complexes. In general, DC conductivity values of the films of **5** and **6** were observed to increase with increasing temperature, suggesting that the compounds are semiconductor in nature (Fig. 7). Conductivity behavior of **5** and **6** can be analyzed in two different temperature regions, low temperature region ( $T \leq 438$  K for **5** and  $T \leq 458$  K for **6**) and high temperature region ( $T > 438$  K for **5** and  $T > 458$  K for **6**). Each region corresponds to a different activation energy with a different slope. This type of behavior can be interpreted as a transition from extrinsic to intrinsic conduction due to the introduced acceptor level within the band gap by impurities such as adsorbed O<sub>2</sub> molecules during the deposition of the films. Activation energy,  $E_{A1}$ , for the low temperature region is associated with a short lived charge transfer between impurity and complex. Activation energy,  $E_{A2}$ , for the higher temperature region, is associated with the resonant energy involved in the short lived excited state.  $E_{A1}$  and  $E_{A2}$  correspond to impurity conduction and an intrinsic generation process, respectively. A similar behavior was reported by Ceyhan et al. [32]. Linear behavior between the DC conductivity and temperature can be represented by the well-known expression (Arrhenius plot) for conductivity [33],

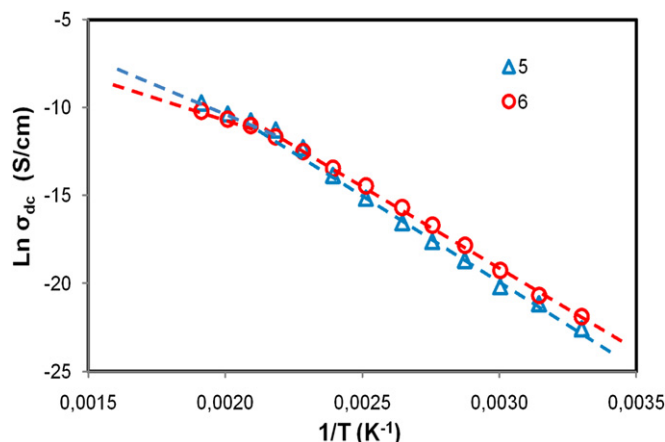


**Fig. 7.** The variation of DC conductivity with temperature for the films of **5** and **6**.

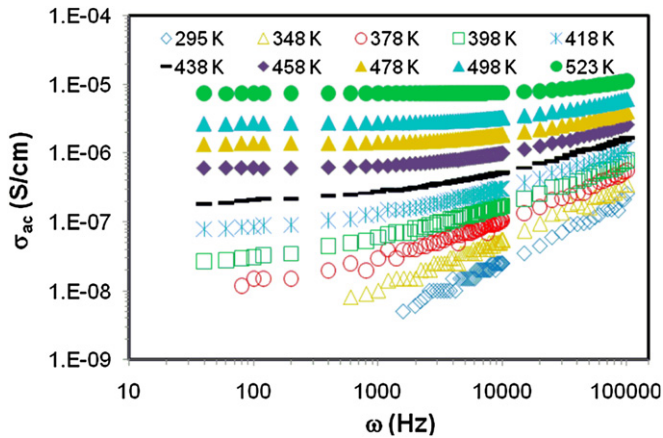


Fig. 8. The variation of AC conductivity with frequency at different temperatures for the film of 6.

$$\sigma_{dc} = \sigma_0 \exp\left(\frac{-E_A}{kT}\right) \quad (1)$$

where  $E_A$  is activation energy,  $T$  is temperature,  $k$  is Boltzman's constant and  $\sigma_0$  is a proportionality constant. The  $E_{A1}$  and  $E_{A2}$  activation energies, determined from the slope of the  $\ln \sigma_{DC}-1/T$  graph, were found to be 0.84 eV ( $T \leq 438$  K) and 0.48 eV ( $T > 438$  K) for **5** and 0.80 eV ( $T \leq 458$  K) and 0.40 eV ( $T > 458$  K) for **6**, respectively. These values are consistent with other reports in different Pc films [34].

### 3.3.2. AC properties

Alternating current (AC) and impedance measurements were carried out on the films of **5** and **6** as a function of frequency in the range of 40 Hz–100 kHz at different temperatures (295 K–523 K) in vacuum ambient ( $\sim 2 \times 10^{-3}$  mbar) in dark. The AC conductivity of **6** was found to increase with increasing temperature and frequency (Fig. 8). While as frequency increases from 40 Hz to  $10^5$  Hz, AC conductivity of **6** increases from  $5.00 \times 10^{-9}$  S/cm (at 1600 Hz) to  $2.55 \times 10^{-7}$  S/cm at room temperature, the values increase from  $7.45 \times 10^{-6}$  S/cm (at 40 Hz) to  $1.12 \times 10^{-5}$  S/cm at 523 K in the measurement frequency range. As in the case of the film **6**, as frequency increases from 40 Hz to  $10^5$  Hz, while AC conductivity of **5** increases from  $5.00 \times 10^{-9}$  S/cm (at 1000 Hz) to  $3.35 \times 10^{-7}$  S/cm at room temperature, the values increase from  $1.98 \times 10^{-5}$  S/cm (at 40 Hz) to  $2.45 \times 10^{-5}$  S/cm at 523 K. In general,  $\sigma_{AC}$  values of **5** were higher than those of **6** at all measurement frequency range and temperatures. The temperature dependence of AC conductivity of the film **6** can also be analyzed in two parts, low temperature region ( $T < 438$  K) and high temperature region ( $T > 438$  K). At the temperatures  $T < 438$  K, its conductivity increases with increasing frequency. At the temperatures  $T > 438$  K, frequency dependence of AC conductivity of the film decreases. The  $\sigma_{AC}$  vs  $\omega$  curves of **5** were similar to those in Fig. 8.

At all temperatures frequency dependence of the measured AC conductivity of the films of **5** and **6** follows a universal power law given by Eq. (2) [35,36],

$$\sigma_{ac} = A\omega^s \quad (2)$$

where  $\omega$  is the angular frequency,  $A$  and  $s$  are material depended constants. To determine the charge transport mechanism involved, the variation of the exponent  $s$  with temperature were examined.  $s$  values were calculated from slope of straight portions of the AC conductivity vs. frequency plot. The variation of  $s$  values with temperature for the films of **5** (inset) and **6** were given in Fig. 9. As

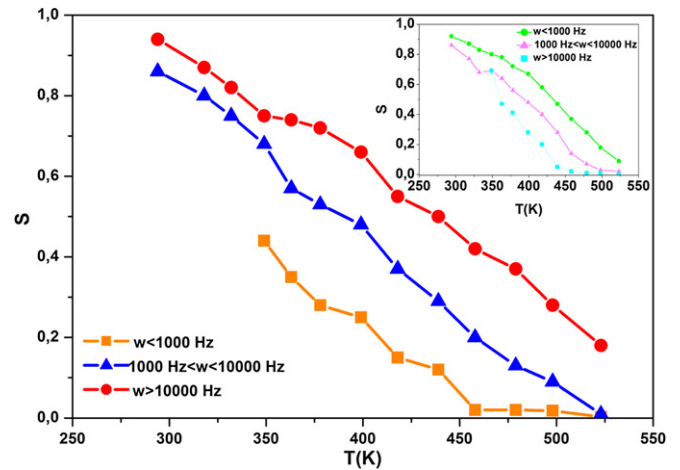


Fig. 9. The variation of  $s$  with temperature for three different frequency regions for the film of **6** (inset for the film of **5**).

seen from this figure,  $s$  values should be analyzed in three different frequency regions, low frequency region ( $\omega < 10^3$  Hz), middle frequency region ( $10^3$  Hz  $< \omega < 10^4$  Hz) and high frequency region ( $10^4$  Hz  $< \omega < 10^5$  Hz). In all frequency regions, temperature dependence of the  $s$  values showed decreasing behavior with temperature. Derived values of  $s$  for the film of **5** take place within the ranges of 0.687–0.006, 0.866–0.003 and 0.908–0.086 for the low, middle and high frequency regions, respectively. The values for the film of **6** are within the ranges of 0.440–0.001, 0.860–0.012 and 0.940–0.178 for the low, middle and high frequency regions, respectively. One important point is the values of  $s$  at the temperatures 458, 478, 498 and 523 K for the films of **5** and **6**. At these temperatures  $s$  values are quite low and the values take place in the range of 0.016 (458 K)–0.006 (523 K) and 0.019 (458 K)–0.001 (523 K) for the films of **5** and **6**, respectively.

The Hopping model predicts a frequency dependent AC conductivity, which increases with the increasing frequency under the condition that, the frequency exponent  $s \leq 1$  [37]. The Hopping model, which was developed by Elliot [37], assumes that charge carriers hop between sites over the potential barrier separating them. The model gives AC conductivity which can be expressed to a first order approximation given by (for single electron hopping),

$$\sigma_{ac}(\omega, T) = \frac{\pi^3 N^2 \epsilon \epsilon_0 \omega}{24} R_w^6 \quad (3)$$

where  $\epsilon$  is the dielectric constant of the material,  $\epsilon_0$  that of free space,  $N$  is the spatial density of defect states and  $R_w$  is the hopping distance. This model predicts a temperature-dependent  $s$  value which is given by,

$$s = 1 - \beta = 1 - \frac{6k_B T}{W_m} \quad (4)$$

where  $k_B$  is Boltzmann's constant and  $W_m$  is the binding energy. In this model  $s$  values decreases with increasing temperature. It is observed that variation of  $s$  values shows a general tendency to decrease with increasing temperature all over the measured frequency range.

According to the Band theory, the AC conductivity should be frequency independent and drops at sufficiently high frequency. In the Quantum-Mechanical Tunneling (QMT) model [38], the component  $s$  is almost equal to 0.8 and increases slightly as temperature increases or is independent of temperature. In this model,  $s$  is given by  $s = 1 + (4/\ln \omega \tau_0)$  where,  $\omega$  is the angular

frequency and  $\tau_0$  the relaxation time of the carrier. So, QMT model is not applicable to our results. According to the Overlapping-Large Polaron Tunneling (QLPT) model [39], the component  $s$  is both frequency and temperature dependent and decreases with increasing temperature to a minimum value at a certain temperature, then it increases with increasing temperature. This model is also not applicable to our results. According to the Small Polaron Quantum Mechanical Tunneling (SP) model, the component  $s$  is an increasing function of temperature [37]. It is also well known that the low values of  $s$  indicate multi-hopping process, while high values of  $s$  indicate single-hopping process.

By comparing the models with our results, charge transport mechanism of the films of **5** and **6** can be interpreted in two parts depending on both temperature and frequency. In the low temperature region ( $T < 458$  K), dominant conduction mechanism can be modeled by single hopping all over the measured frequency range. In the high temperature region ( $T \geq 458$  K) conduction mechanism can be modeled depending on frequency region, i) low frequency region ( $\omega < 1000$  Hz) and ii) high frequency region ( $\omega \geq 1000$  Hz). In the low frequency region, dominant conduction mechanism can be modeled by multi-hopping and in the high frequency region by single hopping.

The impedance data for the films of **5** and **6** were plotted in complex plane (Cole–Cole plot). The complex impedance,  $Z(\omega)$  can be represented as a function of frequency as,

$$Z(\omega) = Z'(\omega) + jZ''(\omega) \quad (5)$$

where  $Z'(\omega)$  and  $Z''(\omega)$  are the real and imaginary parts of impedance. Variation of  $Z''(\omega)$  with  $-Z'(\omega)$  (Nyquist plot) for the film of **5** at different temperatures in the temperature range of 295–523 K were given in Fig. 10. The impedance spectra of the film of **5** consist of a quasi-vertical line up to 438 K. The existence of a semicircular shaped curve in the Nyquist plot means that the impedance becomes capacitive even at relatively high frequency. The curves can be modeled a resistor parallel with a capacitor in series with another resistor [32]. The impedance spectra consist of depressed semicircles with a different radius at the temperatures 438, 458, 478, 498 and 523 K. The temperature effect on impedance spectra can be seen from Fig. 10. The radius of the semicircle decreases with increasing temperature. An ideal semicircle in complex plane only appears in Debye dispersion relations for a single-relaxation time process. Most of the materials show a pronounced deviation from Debye treatment as in our case. In this case, the relaxation time is considered as a distribution of values,

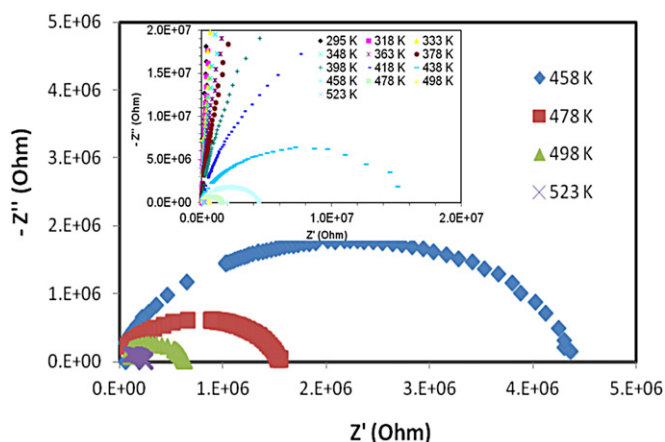


Fig. 10. The Nyquist plot at temperatures  $T \geq 458$  K for the film of **5** (inset for  $295\text{K} \leq T < 458$  K).

rather than a single-relaxation time [40]. The depressed semicircles with different radii indicate deviation from Debye dispersion relation. Therefore, the equivalent circuit is modified to include a constant phase element (CPE). The series resistance in the equivalent circuit represents the ohmic losses in the test fixture and electrode sheet resistance. The parallel resistance is of the coating material in parallel with that of the substrate. The intercepts of the semicircular arcs with real axis give us an estimate of the bulk resistance of the material. It is observed that bulk resistance decreases with increasing temperature indicating semiconductor property. The existence of the CPE represents a slight distribution of relaxation times instead of a discrete relaxation time. This interpretation was consistent with  $Z$  versus  $\omega$  plot (Bode plot). The Bode plots for the films of **5** and **6** (inset) are shown in Fig. 11.

As temperature increases from 295 K to 418 K, the slope of  $\log Z$  versus  $\log \omega$  curves varies from  $-0.989$  to  $-0.921$ . It appears that the film exhibits capacitive behavior between the temperatures of 295–418 K. The slope of the curves in the frequency range of  $10^4$ – $10^5$  Hz takes the values  $-0.678$ ,  $-0.478$  and  $-0.250$  at the temperatures 478, 498 and 523 K, respectively. The results also indicate the existence of a CPE [32]. Similar results of the Bode plot were found for the film of **6** (inset in Fig. 11). The complex impedance spectrum of **6** was also similar to those in Fig. 10.

### 3.4. Electrochemical and in situ spectroelectrochemical measurements

The electrochemical behavior of  $\alpha$ -tetra substituted coumarinoxy Pcs **4–6** was investigated by cyclic voltammetry, differential pulse voltammetry and *in situ* spectroelectrochemistry in DMSO and DCM involving tetrabutylammonium perchlorate (TBAP) as supporting electrolyte. The voltammetric data of the complexes, including the half-wave redox potential value ( $E_{1/2}$ ), anodic-to-cathodic peak potential separation ( $\Delta E_p$ ) and the difference between the first oxidation and reduction potential ( $\Delta E_{1/2}$ ) are summarized in Table 3. The peak currents for the redox couples of the complexes were usually found to be directly proportional to the square root of scan rate, suggesting their diffusion-controlled nature.

Compound **4** displayed three reduction couples (R1–R3) and an oxidation couple (O1) in DMSO/TBAP (Supplementary material, Fig. S12). These processes are clearly Pc ring-based, except the third reduction process (R3) which could be monitored only by differential pulse voltammetry. The R3 process occurs at remarkably negative potentials and probably corresponds to the reduction of 7-oxy-4-(4-methoxyphenyl)-8-methylcoumarin substituents since these groups, less conjugated as compared with the Pc ring, are

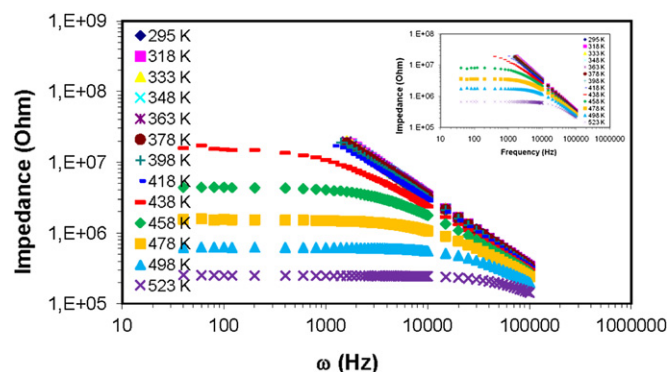


Fig. 11. The variation of impedance with frequency for the film of **5** at different temperatures (inset for the film of **6**).

**Table 3**  
Voltammetric data for  $\alpha$ -tetra-7-oxy-4-(4-methoxyphenyl)-8-methylcoumarin substituted Pcs **4–6**.

Complex	Ring Oxidations	M <sup>II</sup> /M <sup>III</sup>	M <sup>II</sup> /M <sup>I</sup>	Ring reductions	$f\Delta E_{1/2}$	
<b>4</b> (H <sub>2</sub> Pc) in DMSO	<sup>a</sup> $E_{1/2}$ (V)	0.49		–0.48	–0.86	<sup>d,e</sup> –1.64
	<sup>b</sup> $\Delta E_p$ (V)	0.070		0.060	0.080	<sup>d</sup> rev
<b>5</b> (CoPc) in DMSO	<sup>a</sup> $E_{1/2}$ (V)	0.49	–0.29	–1.23	–1.65	
	<sup>b</sup> $\Delta E_p$ (V)	0.080	0.100	0.100	<sup>d</sup> rev	0.78
<b>5</b> (CoPc) in DCM	<sup>a</sup> $E_{1/2}$ (V)	0.65	–0.20	–1.29		0.85
	<sup>b</sup> $\Delta E_p$ (V)	0.060	0.080	0.100		
<b>6</b> (ZnPc) in DMSO	<sup>a</sup> $E_{1/2}$ (V)	0.85		–0.68	–0.96	–1.31
	<sup>b</sup> $\Delta E_p$ (V)	0.100		0.080	0.120	–
<b>6</b> (ZnPc) in DCM	<sup>a</sup> $E_{1/2}$ (V)	0.88		<sup>c</sup> –0.20 (–0.64)	<sup>c</sup> –0.96	<sup>c</sup> –1.30
	<sup>b</sup> $\Delta E_p$ (V)	0.080		<sup>c</sup> rev (rev)	<sup>c</sup> rev	<sup>c</sup> rev

<sup>a</sup>  $E_{1/2} = (E_{pa} + E_{pc})/2$  at 0.025 V s<sup>–1</sup>.

<sup>b</sup>  $\Delta E_p = E_{pa} + E_{pc}$  at 0.025 V s<sup>–1</sup>.

<sup>c</sup>  $E_{1/2}$  and  $\Delta E_p$  could not be determined due to ill-defined cyclic voltammetry waves, associated with aggregation-deaggregation equilibria, however, the shape of the differential pulse voltammograms implied reversible electron transfer.

<sup>d</sup>  $E_{1/2}$  could be determined only by differential pulse voltammetry. The shape of the differential pulse voltammogram confirmed the reversibility of electron transfer process.

<sup>e</sup> It corresponds probably to the reduction of coumarin substituent.

<sup>f</sup>  $\Delta E_{1/2} = E_{1/2}$  (first oxidation) –  $E_{1/2}$  (first reduction). This value corresponds to the HOMO–LUMO gap for metal-free and metallophthalocyanines having electro-inactive metal center, but it represents metal to ligand (MLCT) or ligand to metal (LMCT) charge transfer transition gap for metallophthalocyanines having redox active metal center.

expected to be reduced at relatively more negative potentials. The cathodic to anodic peak current ratio of the first reduction process was observed to increase with increasing potential scan rate, indicating that electrochemically produced radical cations are not stable electrochemically. Fig. 12A shows the cyclic voltammograms

of  $5.00 \times 10^{-4}$  M **6** at different scan rates in DMSO/TBAP. It shows four reduction processes (R1–R4) and an oxidation couple (O1). The redox-inactive nature of metal center in zinc Pcs is very clear from previous literature [41]. R1–R3 and O1 processes can be attributed to successive addition of electrons to, and removal of an electron from the macrocycle orbitals, respectively [42]. The process R4, appearing at high negative potentials at the end of solvent-limited cathodic potential range, probably corresponds to the reduction of 7-oxy-4-(4-methoxyphenyl)-8-methylcoumarin substituents since the currents for this process occurring at the same potential are much higher than those of the other Pc-based one-electron ones. In fact, the current for this process is expected to be four times higher than that of the other Pc-based one-electron ones. However, it was not possible to check this proportionality exactly, due to the ill-defined process appearing at high negative potentials. The comparison of the two groups of cyclic voltammograms at different scan rates in Fig. 12A suggests that the shape of the O1 couple is strongly affected by the switching potential at the cathodic side. The Pc-based redox processes of oxy-coumarin substituted **6** in DMSO/TBAP occur at remarkably more positive potentials than those of various unsubstituted [42] and RO-substituted zinc(II) Pcs [43–46] due to the electron-withdrawing character of 7-oxy-4-(4-methoxyphenyl)-8-methylcoumarin moieties. *In situ* spectroelectrochemical measurements were also carried out during the controlled-potential electrolysis of **6** in DMSO at a suitable potential corresponding to its first reduction process since this type of measurements do not only have a vital importance in determining the nature of the redox processes, but also provide support for the evaluation of the aggregation effect on the redox processes. The spectral changes during the first reduction process of **6** at –0.85 V vs. SCE are shown in Fig. 12B. As shown in this figure, the association of electron transfer process with aggregation is excluded by a sharp Q absorption band in the spectrum of **6** in DMSO/TBAP at the beginning of electrolysis. During the controlled-potential electrolysis at –0.85 V vs. SCE, a decrease in the absorptions of the Q band centered at 695 nm and the vibrational band at 625 nm is observed without shift. At the same time, the absorption of the B band at 320 nm decreases without shift and a new band appears at 556 nm. Well-defined isosbestic points are observed at 282, 428, 604 and 726 nm. These spectral changes, especially the formation of a new band at 556 nm, are typical for Pc ring reduction, and thus, the formation of [Zn(II)Pc(–3)]<sup>–</sup> species [47,48]. Therefore, the first reduction process of **6** is assigned to Pc(–2)/Pc(–3) electron transfer process which is not associated by aggregation-deaggregation equilibrium.

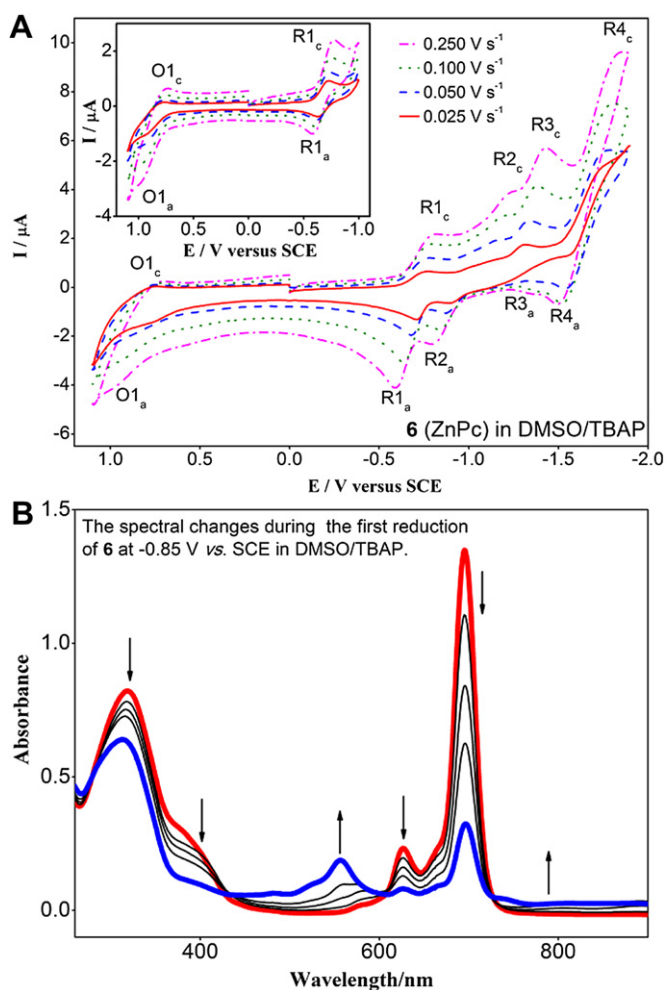


**Fig. 12.** Cyclic voltammograms (A) and *in situ* UV–vis spectral changes during the first reduction (B) of **6**.

Fig. 13A shows the cyclic and differential pulse (inset) voltammograms of  $5.00 \times 10^{-4}$  mol dm $^{-3}$  **6** in a non-coordinating solvent medium, DCM/TBAP. It also shows four reduction processes (R1–R4) and an oxidation couple (O1) in DCM/TBAP. However, the first reduction process is split into two reduction couples (R1' and R1''). Thus, it occurs at less negative potentials than those in DMSO/TBAP. The first oxidation process in DCM/TBAP is observed at similar potentials to those in DMSO/TBAP. It appears that the non-coordinating solvent DCM makes the first reduction process of **6** easier, probably as a result of the increasing interaction between the metal center of a Pc molecule and the oxygen atoms in another Pc molecule, and thus remarkable stabilization of the LUMO energy level. It appears that the mentioned interactions between the ZnPc molecules lead to the establishment of equilibrium between monomer and J-aggregated species. In the light of this evaluation, the R1' and R1'' processes can be attributed to the reduction of J-aggregated and monomeric species, respectively. The presence of equilibrium between monomer and J-aggregated species of **6** in DCM/TBAP was confirmed clearly by the split Q band in its electronic absorption spectrum (Fig. 13B). Fig. 13B shows the former spectral changes during the application of  $-0.80$  V vs. SCE. The absorption of the J-band at 741 nm decreases without shift and finally disappears while the absorption of the Q band at 692 nm increases. The first group of spectral changes is followed by decrease in the absorptions of the bands at 692, 622, 400 and 316 nm without shift and increase in the absorption between 500 and 600 nm (Fig. 13C). This second group of spectral changes are typical for a Pc(-2)/Pc(-3) reduction process. The two groups of spectral changes in Fig. 13B and C suggest clearly that in DCM/TBAP,

J-aggregated species of **6** deaggregates before the first reduction process. The spectral changes during the second reduction process of **6** at  $-1.00$  V vs. SCE are shown in Fig. 13D. As shown in this figure, the absorptions of the bands at 692, 662, 622 and 589 nm decrease without shift whereas the intensity of the band at 587 nm increases also without shift. These spectral changes are characteristic for a Pc(-3)/Pc(-4) reduction process. On the basis of the well-known electrochemical behavior of metal Pcs involving redox-inactive metal center [42], the R3 couple corresponds to the third reduction process of Pc(-4)/Pc(-5). Although the peak currents of R4 couple appearing at remarkably negative potentials at the end of solvent-limited cathodic potential range are comparable to those of other Pc-based couples, the remarkably higher peak currents of R4 in the differential pulse voltammogram in the inset in Fig. 13A implies that it can be attributed to the four-electron reduction of four substituents at the same potential.

Fig. 14A shows the cyclic and differential pulse (inset) voltammograms of **5** (CoPc) in DMSO/TBAP. The complex **5** undergoes three reductions (R1, R2 and R3) and an oxidation (O1) within the available potential range. As shown in the inset, the R3 couple could be monitored only by differential pulse voltammetry. Co(II) center in **5** may have accessible d orbital levels lying between the HOMO and LUMO gap of the Pc ligand, depending on whether there are any available coordinating species that would stabilize it, and thus, can be oxidized and reduced before the ring-based redox processes. For this reason, spectroelectrochemical measurements were also carried out to assign the redox processes of **5**, especially the first reduction and the first oxidation. The complex **5** does not aggregate in TBAP/DMSO as evidenced from the narrow Q band at 677 nm in

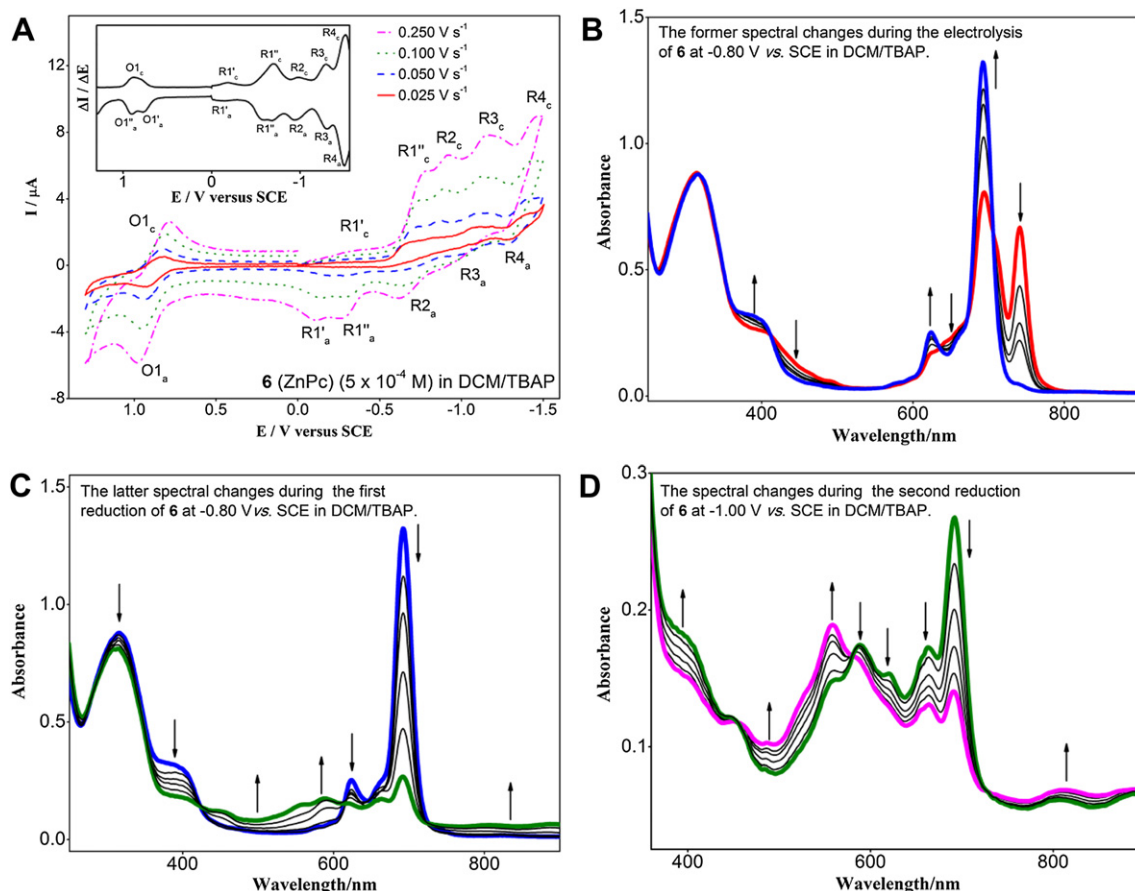
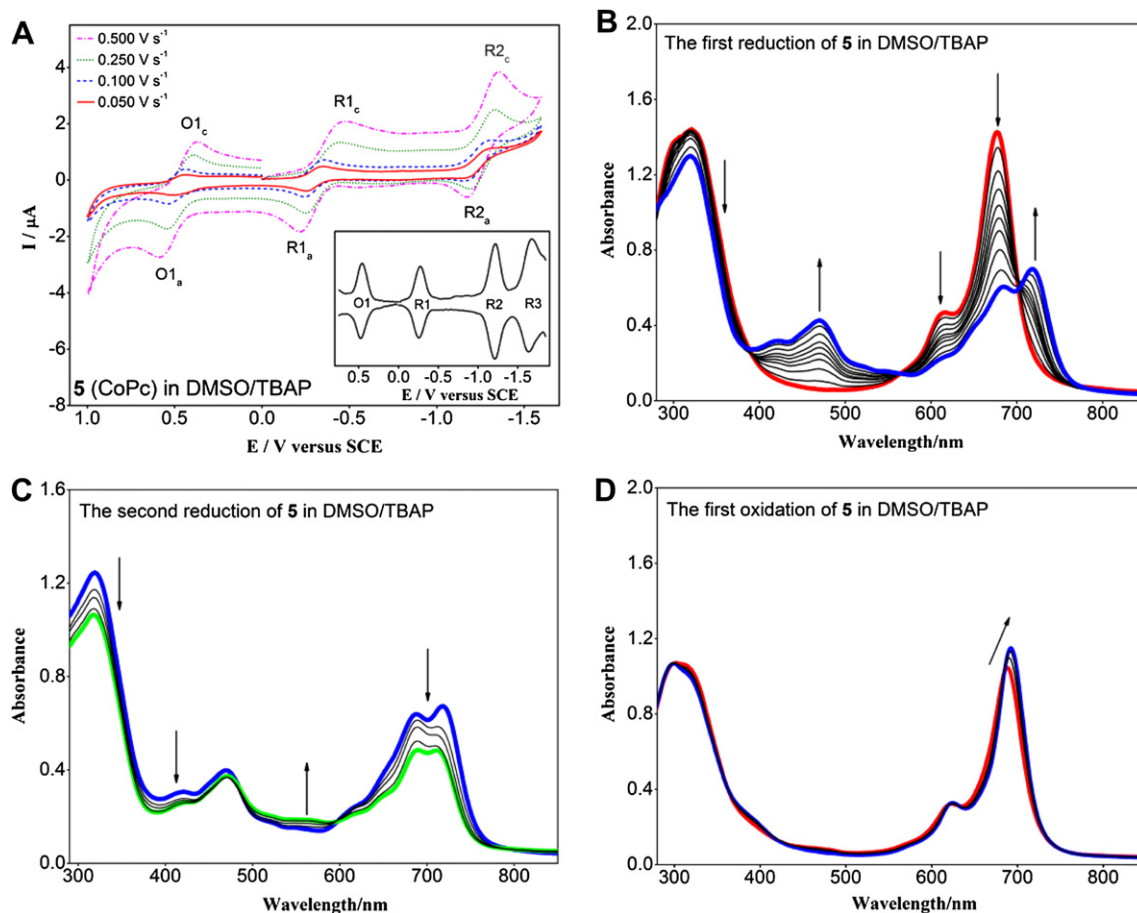


Fig. 13. Cyclic and differential pulse (inset) voltammograms of **6** (A) and *in situ* UV-vis spectral changes during the electrolysis of **6** at various constant potentials (B–D).



**Fig. 14.** Cyclic and differential pulse (inset) voltammograms of **5** (A) and *in situ* UV–vis spectral changes during the redox processes of **5** at various constant potentials (B–D) in DMSO/TBAP.

its original absorption spectra in Fig. 14B which also shows the spectroscopic changes observed across the first reduction of **5** in DMSO/TBAP. With the progress of electrolysis, the Q band nearly fades away and a new Q band, which has approximately half the intensity of the original Q band, develops at longer wavelength, accompanied by formation of a new band at 476 nm in the region between the Q and Soret bands. A set of isosbestic points was detected at four wavelengths. These are similar to the changes observed to date for many CoPc derivatives when Co(II) was reduced to Co(I), and the band developed between the Q and Soret bands has been assigned to an metal-to-ligand charge transfer (MLCT) process from cobalt  $e_g$  to ligand  $b_{1u}$  and  $b_{2u}$  orbitals under  $D_{4h}$  symmetry [49–51]. Thus, it is very clear that the first reduction is occurring at cobalt. During the second reduction, the Q bands at 686 and 718 nm decreased without shift (Fig. 14C) while the absorption between 500 and 600 nm increased and a new weak band at 564 nm appeared. These spectral changes at the potential of the couple R2 are characteristic for a ring-based reduction in Co(II) Pc complex,  $[\text{Co(I)Pc(-2)}]^- / [\text{Co(I)Pc(-3)}]^{2-}$ . The subsequent third reduction is also expected to be on the ring in comparison with literature [42]. Fig. 14D displays the spectral changes during the first oxidation process. The Q band at 677 nm increases in intensity with red shift to 683 nm. The increase of the Q band with red shift is typical of a metal-based oxidation in CoPc complexes, and thus, indicates clearly that the O1 couple of **5** corresponds to  $\text{Co(II)Pc(-2)} / [\text{Co(III)Pc(-2)}]^+$  process [52–54].

The reduction behavior of **5** in DMSO/TBAP and DCM/TBAP is very similar (Figs. 14A and 15A). However, it displays two oxidation

couples in DCM/TBAP while it shows only one oxidation couple in DMSO/TBAP within the available potential ranges. The first oxidation process of **5** in DCM/TBAP occurs at more positive potentials than that in DMSO/TBAP. Contrary to that in DMSO/TBAP, the first oxidation couple in DCM/TBAP is probably ring-based whereas the second oxidation process of **5** in DCM/TBAP should correspond to Co(II)/Co(III) couple [42]. Fig. 15B displays the UV–vis spectrum of **5** in DCM/TBAP and *in situ* spectral changes during its first reduction at  $-0.60$  V vs. SCE. As shown in this figure, the solution of complex **5** in DCM/TBAP does not involve H- or J-aggregated species as understood clearly from the narrow and non-split Q band at 683 nm. The absorption of the Q band at 683 nm decreases and a new Q band develops at longer wavelength. These spectral changes at  $-0.60$  V vs. SCE are accompanied by the formation of a new band at 471 nm which is assigned to an MLCT process from cobalt  $e_g$  to ligand  $b_{1u}$  and  $b_{2u}$  orbitals under  $D_{4h}$  symmetry when Co(II) is reduced to Co(I) [49–51]. During the second reduction, the Q bands at 649, 686 and 712 nm decreases without shift while the absorption between 500 and 600 nm increases, and a new band at this region appears (Fig. 15C). These spectral changes at the potential of the couple R2 are characteristic for a ring-based reduction in Co(II)Pc complex,  $[\text{Co(I)Pc(-2)}]^- / [\text{Co(I)Pc(-3)}]^{2-}$ . Fig. 15D displays *in situ* UV–vis spectral changes during the first oxidation process of **5** at  $0.85$  V vs. SCE in DCM/TBAP. The absorption of the Q band at 683 nm decreases without shift and a new band forms at 538 nm. These spectral changes are characteristic for a Pc-based oxidation and thus, lead to the formation of  $[\text{Co(II)Pc(-1)}]^+$  species [47,48]. Unfortunately, the controlled-potential

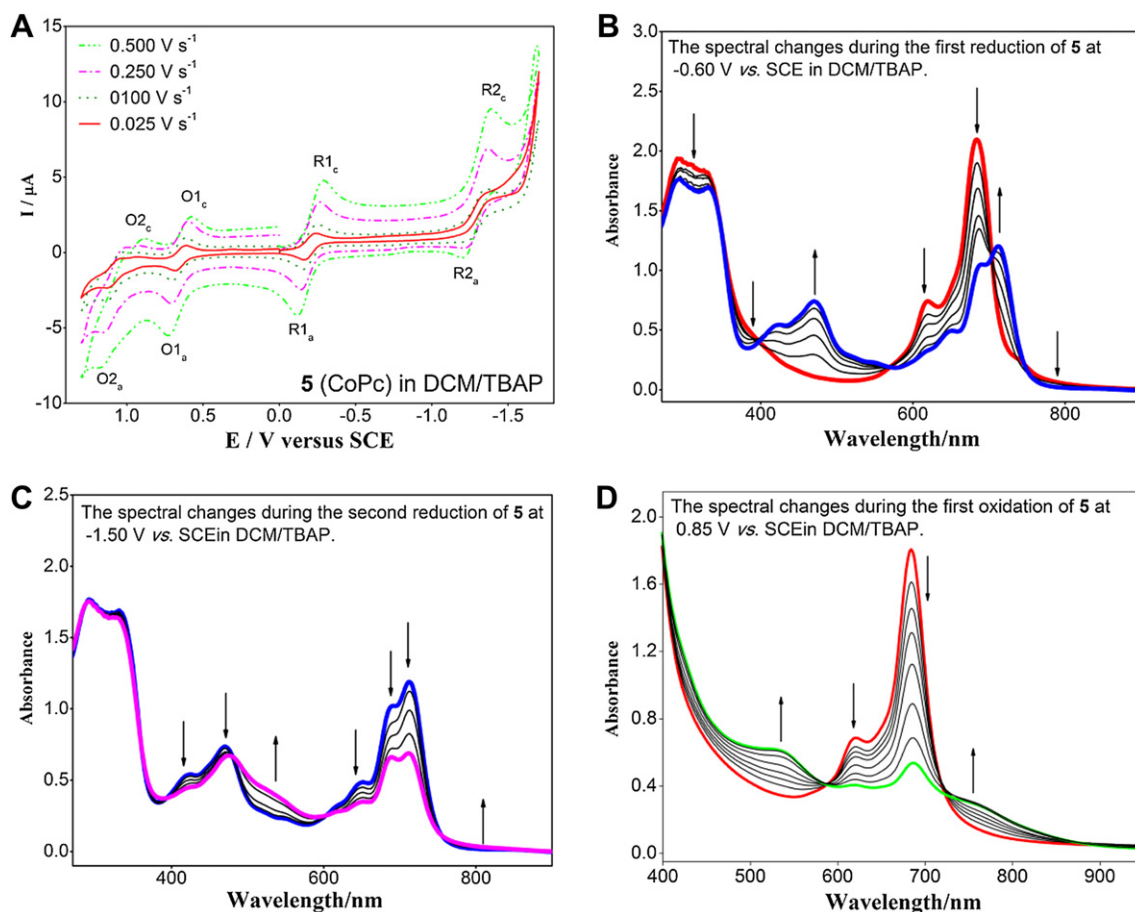


Fig. 15. Cyclic voltammograms of **5** (A) and *in situ* UV–vis spectral changes during the redox processes of **5** at various constant potentials (B–D) in DCM/TBAP.

electrolysis of **5** at the potentials more positive than 1.20 V vs. SCE in DCM/TBAP resulted in decomposition of the complex under the conditions of constant-potential electrolysis, as evidenced from decrease in the absorption of all peaks. However, the previous studies on the redox behavior of Co(II) Pcs suggest that the second oxidation of **5** in DCM is metal-based and thus, can be assigned to  $[\text{Co(II)Pc(-1)}]^+ / [\text{Co(III)Pc(-1)}]^{2+}$  redox couple [42].

#### 4. Conclusion

The novel  $\alpha$ -tetra substituted metal free Pc (**4**), cobalt(II) Pc (**5**) and zinc(II) Pc (**6**) have been synthesized from 3-[4-(4-methoxyphenyl)-8-methylcoumarin-7-oxy]phthalonitrile (**3**). The complexes were characterized by elemental analysis, UV–vis, IR,  $^1\text{H}$  NMR,  $^{13}\text{C}$  NMR and MALDI-TOF mass spectroscopies. It was concluded from the investigation of the spectroscopic behavior of these novel compounds in various solvents that complex **6** forms J-aggregates in non-coordinating solvents such as chloroform, DCM and toluene, as a result of the complementary coordination of the oxygen atoms in the macrocycle of one molecule to the core zinc atom of another molecule. The observed J-aggregates were broken up by the addition of a coordinating solvent such as DMSO.

The photophysical and photochemical properties of metal-free (**4**), cobalt (**5**) and zinc (**6**) Pc complexes were described in different solvents (toluene, chloroform, DCM and DMSO) for comparison. Complex **6** showed good singlet oxygen generation which gives an indication of its potential usability as photosensitizer in photocatalytic applications such as photodynamic therapy.

In general, DC conductivity of the films of **5** and **6** was observed to increase with increasing temperature and display Arrhenius behavior with activation energies varying within the range of 0.40–0.84 eV depending on temperature regions. The evaluation of the AC conductivity measurements suggested that the charge transport mechanism in their films can be explained by a hopping model.

Electrochemical and *in situ* spectroelectrochemical measurements of the complexes showed that **4** and **6** display Pc ring-based redox processes whereas **5** display both metal and Pc ring-based processes. In DMSO, the oxidation of the Co(II) center in **5** occurs before that of Pc ring, probably as a result of its coordination at axial positions by the solvent molecules while the order of the oxidation processes changes in DCM which is non-coordinating. In DCM, the first reduction and oxidation couples of **6** are split due to the presence of J-aggregates and the equilibrium between monomeric and aggregated species.

#### Acknowledgment

We are thankful to The Foundation of Marmara University and The Commission of Scientific Research (BAPKO) (Project No: FEN-A-090909-0302).

#### Appendix A. Supplementary material

Supplementary data associated with this article can be found, in the online version, at <http://dx.doi.org/10.1016/j.dyepig.2012.05.021>.

## References

- [1] Tanaka M. Phthalocyanines. In: Faulkner EB, Schwartz RJ, editors. High performance pigments and their applications. Weinheim-Germany: Wiley-VCH; 2009. p. 276–90.
- [2] O'Regan BC, Duarte IL, D'Á MVM, Forneli A, Albero J, Morandeira A, et al. Catalysis of recombination and its limitation on open circuit voltage for dye sensitized photovoltaic cells using phthalocyanine dyes. *J Am Chem Soc* 2008; 130:2906–7.
- [3] Koç I, Özer M, Özkaya AR, Bekaroğlu Ö. Electrocatalytic activity, methanol tolerance and stability of perfluoroalkyl-substituted mononuclear, and ball-type dinuclear cobalt phthalocyanines for oxygen reduction in acidic medium. *Dalton Trans* 2009;32:6368–76.
- [4] Koca A, Ceyhan T, Erbil MK, Özkaya AR, Bekaroğlu Ö. Electrochemistry and spectroelectrochemistry of tert-butylcalix[4]arene bridged bis double-decker lutetium(III) phthalocyanine, Lu<sub>2</sub>Pc<sub>4</sub> and dimeric lutetium(III) phthalocyanine, Lu<sub>2</sub>Pc<sub>2</sub>(OAc)<sub>2</sub>. *Chem Phys* 2007;340:283–92.
- [5] Huang X, Zhao F, Li Z, Tang Y, Zhang F, Tung CH. Self-assembled nanowire networks of aryloxy zinc phthalocyanines based on Zn-O coordination. *Langmuir* 2007;23:5167–72.
- [6] Snow AW. In: Kadish KM, Smith KM, Guillard R, editors. The porphyrin handbook, vol. 17. San Diego: Academic; 2003. p. 37–119.
- [7] George RD, Snow AW, Shirk JS, Barger WR. The alpha substitution effect on phthalocyanine aggregation. *J Porphyr Phthalocya* 1998;2:1–7.
- [8] Sessler JL, Jayawickramarajah J, Gouloumis A, Pantos GD, Torres T, Guldi DM. Guanidine and fullerene derived de-aggregation of a new phthalocyanine-linked cytidine derivative. *Tetrahedron* 2006;62:2123–31.
- [9] Ng ACH, Li XY, Ng DKP. Synthesis and photophysical properties of non-aggregated phthalocyanines bearing dendritic substituents. *Macromolecules* 1999;32:5292–8.
- [10] Law KY. Effect of dye aggregation on the photogeneration efficiency of organic photoconductors. *J Phys Chem* 1988;92:4226–31.
- [11] Louati A, El Meray M, Andre JJ, Simon J, Kadish KM, Gross M, et al. Electrochemical reduction of new, good electron-acceptors - the metallooctacyanophthalocyanines. *Inorg Chem* 1985;24:1175–9.
- [12] Durmuş M, Nyokong T. Synthesis and solvent effects on the electronic absorption and fluorescence spectral properties of substituted zinc phthalocyanines. *Polyhedron* 2007;26:2767–76.
- [13] Kameyama K, Morisue M, Satake A, Kobuke Y. Highly fluorescent self-coordinated phthalocyanine dimers. *Angew Chem* 2005;44:4763–6.
- [14] Kotali A, Lafazanis IS, Haris PA. A novel and facile synthesis of 7,8-diacoumarins. *Tetrahedron Lett* 2007;48:7181–3.
- [15] Ye FF, Gao JR, Sheng WJ, Jia JH. One-pot synthesis of coumarin derivatives. *Dyes Pigm* 2008;77:556–8.
- [16] Alemdar A, Özkaya AR, Bulut M. Preparation, characterization, electrochemistry and in situ spectroelectrochemistry of novel alpha-tetra[7-oxo-3-(2-chloro-4-fluorophenyl)coumarin]-substituted metal-free, cobalt and zinc phthalocyanines. *Synth Met* 2010;160:1556–65.
- [17] Alemdar A, Özkaya AR, Bulut M. Synthesis, spectroscopy, electrochemistry and in situ spectroelectrochemistry of partly halogenated coumarin phthalonitrile and corresponding metal-free, cobalt and zinc phthalocyanines. *Polyhedron* 2009;28:3788–96.
- [18] Dur E, Özkaya AR, Bulut M. Synthesis, characterisation and electrochemistry of derivatisable novel  $\alpha$ -tetra 7-oxycoumarin-3-carboxylate-substituted metallo-phthalocyanines. *Supramol Chem* 2011;23:379–88.
- [19] Özer M, Altındal A, Özkaya AR, Salih B, Bulut M, Bekaroğlu Ö. Synthesis, characterization, and electrochemical and electrical properties of novel pentaerythritol-bridged cofacial bismetallophthalocyanines and their water-soluble derivatives. *Eur J Inorg Chem* 2007;22:3519–26.
- [20] Çamur M, Özkaya AR, Bulut M. Synthesis, characterization and spectroscopic properties of new fluorescent 7,8-dihexyloxy-3-(4-oxophenyl)coumarin substituted phthalocyanines. *J Porphyr Phthalocya* 2009;13:691–701.
- [21] Bilgiçli AT, Kandaz M, Özkaya AR, Salih B. Tetrakis-phthalocyanines bearing electron-withdrawing fluoro functionality: synthesis, spectroscopy, and electrochemistry. *Heteroatom Chem* 2009;20:262–71.
- [22] Yüksel F, Gürek AG, Lebrun C, Ahsen V. Synthesis and solvent effects on the spectroscopic properties of octatosylamido phthalocyanines. *New J Chem* 2005;29:726–32.
- [23] Minnes R, Weltman H, Lee HJ, Gorun SM, Ehrenberg B. Enhanced acidity, photophysical properties and liposome binding of perfluoroalkylated phthalocyanines lacking C-H bonds. *Photochem Photobiol* 2006;82:593–9.
- [24] Chen Z, Zhong C, Zhang Z, Li Z, Niu L, Bin Y, et al. Photoresponsive J-aggregation behavior of a novel azobenzene-phthalocyanine dyad and its third-order optical nonlinearity. *J Phys Chem B* 2008;112:7387–94.
- [25] Qi ZM, Zhou HS, Honma I, Itoh K, Yanangi H. A disposable ozone sensor based on a grating-coupled glass waveguide coated with a tapered film of copper tetra-*t*-butylphthalocyanine. *Sens Actuators B* 2005;106:278–83.
- [26] Nyokong T. Effects of substituents on the photochemical and photophysical properties of main group metal phthalocyanines. *Coord Chem Rev* 2007;251:1707–22.
- [27] Maree MD, Nyokong T, Suhling K, Phillips D. Effects of axial ligands on the photophysical properties of silicon octaphenoxypthalocyanine. *J Porphyr Phthalocya* 2002;6:373–6.
- [28] Zorlu Y, Dumoulin F, Durmuş M, Ahsen V. Comparative studies of photophysical and photochemical properties of solketal substituted platinum(II) and zinc(II) phthalocyanine sets. *Tetrahedron* 2010;66:3248–58.
- [29] Achar BN, Mohan-Kumar TM, Lokesh KS. Synthesis, characterization, pyrolysis kinetics and conductivity studies of chloro substituted cobalt phthalocyanines. *J Coord Chem* 2007;60:1833–46.
- [30] Kamimura K, Muto J, Akiyama K. Electrical and structural-properties of orthochloranil doped zinc phthalocyanine films. *J Mater Sci-Mater Electron* 1991;2:244–7.
- [31] Saleh AM, Abu-Hilal AO, Gould RD. Investigation of electrical properties (AC and DC) of organic zinc phthalocyanine, ZnPc, semiconductor thin films. *Curr Appl Phys* 2003;3:345–50.
- [32] Ceyhan T, Altındal A, Erbil MK, Bekaroğlu Ö. Synthesis, characterization, conduction and gas sensing properties of novel multinuclear metallo phthalocyanines (Zn, Co) with alkylthio substituents. *Polyhedron* 2006;25:737–46.
- [33] Sülü M, Altındal A, Bekaroğlu Ö. Synthesis, characterization and electrical and CO<sub>2</sub> sensing properties of triazine containing three dendritic phthalocyanine. *Synth Met* 2005;155:211–21.
- [34] Canlıca M, Altındal A, Özkaya AR, Salih B, Bekaroğlu Ö. Synthesis, characterization, and electrochemical, and electrical measurements of novel 4,4'-isopropylidendiaryldiphenyl bridged bis and cofacial bis-metallophthalocyanines (Zn, Co). *Polyhedron* 2008;27:1883–90.
- [35] Mott NF, Davis EA. *Electronic processes in non-crystalline materials*. 2nd ed. Oxford: Clarendon Press; 1979.
- [36] Lee WK, Liu JF, Nowick AS. Limiting behavior of AC conductivity in ionically conducting crystals and glasses - a new universality. *Phys Rev Lett* 1991;67:1559–61.
- [37] Elliott SR. AC conduction in amorphous-chalcogenide and pnictide semiconductors. *Adv Phys* 1987;36:135–218.
- [38] Ghosh A. Frequency-dependent conductivity in bismuth-vanadate glassy semiconductors. *Phys Rev B* 1990;41:1479–88.
- [39] Long AR. Frequency-dependent loss in amorphous-semiconductors. *Adv Phys* 1982;31:553–637.
- [40] Chen YJ, Zhang XY, Cai TY, Li ZY. Temperature dependence of AC response in diluted half-metallic CrO<sub>2</sub> powder compact. *J Alloy Comp* 2004;379:240–6.
- [41] George RD, Snow AW. Synthesis of 3-nitrothalonitrile and tetra-alpha-substituted phthalocyanines. *J Heterocyclic Chem* 1995;32:495–8.
- [42] Milaeva ER, Speier G, Lever ABP. The redox chemistry of metallophthalocyanines. In: Leznoff CC, Lever ABP, editors. *Phthalocyanines: properties and applications*, vol. 3. New York: VCH; 1993. p. 1–69.
- [43] Çamur M, Durmuş M, Özkaya AR, Bulut M. Synthesis, photophysical, photochemical and electrochemical properties of crown ether bearing coumarin substituted phthalocyanines. *Inorg Chim Acta* 2012;383:287–99.
- [44] Erdoğan A, Koca A, Uğur AL, Erden İ. Synthesis, electrochemical and spectroelectrochemical properties of highly soluble tetra substituted phthalocyanines with [4-(thiophen-3-yl)-phenoxy]. *Synth Met* 2011;161:1319–29.
- [45] Kandaz M, Yaraşır MN, Koca A. Selective metal sensor phthalocyanines bearing non-peripheral functionalities: synthesis, spectroscopy, electrochemistry and spectroelectrochemistry. *Polyhedron* 2009;28:257–62.
- [46] Biyıklıoğlu Z, Çakır V, Koca A, Kantekin H. Synthesis, electrochemical, in-situ spectroelectrochemical and in-situ electrochromic characterization of non-peripheral tetrasubstituted metal-free and metallophthalocyanines. *Dyes Pigm* 2011;89:49–55.
- [47] Mack J, Stillman MJ. Photochemical formation of the anion-radical of zinc phthalocyanine and analysis of the absorption and magnetic circular-dichroism spectral data-assignment of the optical-spectrum of [ZnPc<sup>-3</sup>]. *J Am Chem Soc* 1994;116:1292–304.
- [48] Nyokong T, Gasyna Z, Stillman M. Phthalocyanine Pi-Cation-Radical species - Photochemical and electrochemical Preparation of [ZnPc<sup>-1</sup>]<sup>+</sup> in solution. *Inorg Chem* 1987;26:548–53.
- [49] Hesse K, Schlettwein D. Spectroelectrochemical investigations on the reduction of thin films of hexadecafluorophthalocyaninatozinc (F<sub>16</sub>PcZn). *J Electroanal Chem* 1999;476:148–58.
- [50] Özer M, Altındal A, Özkaya AR, Bulut M, Bekaroğlu Ö. Synthesis, characterization and some properties of novel bis(pentafluorophenyl)methoxyl substituted metal free and metallophthalocyanines. *Polyhedron* 2006;25:3593–602.
- [51] Koca A, Özkaya AR, Arslanoğlu Y, Hamuryudan E. Electrochemistry, spectroelectrochemistry and electrochemical polymerization of titanilphthalocyanines. *Electrochim Acta* 2007;52:3216–21.
- [52] Osmanbaş OA, Koca A, Özçesmeçi İ, Okur Aİ, Gül A. Voltammetric, spectroelectrochemical, and electrocatalytic properties of thiol-derivatized phthalocyanines. *Electrochim Acta* 2008;53:4969–80.
- [53] Koca A, Özkaya AR, Selçukoğlu M, Hamuryudan E. Electrochemical and spectroelectrochemical characterization of the phthalocyanines with pentafluorobenzyloxy substituents. *Electrochim Acta* 2007;52:2683–90.
- [54] Jin Z, Nolan K, McArthur CR, Lever ABP, Leznoff CC. Synthesis, electrochemical and spectroelectrochemical studies of metal-free 2,9,16,23-tetraferrocenylphthalocyanine. *J Organomet Chem* 1994;468:205–12.